FlyEyes: A CCD-based detector for CFHT's AO system

Olivier Lai[a], Kevin K.Y. Ho[a], Marc Baril[a], Jean-Charles Cuillandre[a], Chueh-Jen Lin[b], Tom Benedict[a], Jeff Ward[a], Derrick Salmon[a], Gerry Luppino[c], James Beletic[d], Reinhold Dorn[e], Pascal Puget[f], Barry Burke[g], Shiang-Yu Wang[b],

[a] Canada France Hawaii Telescope, Kamuela, HI, USA
[b] Institute for Astronomy and Astrophysics, National Taiwan University, Taipei, Taiwan, R.O.C.
[c] Institute for Astronomy, University of Hawaii, Honolulu, HI, USA
[d] Rockwell Scientific Company, Thousand Oaks, CA , USA
[e] European Southern Observatory, Garching, Germany
[f]Observatoire de Paris, Meudon, France
[g] MIT Lincoln Laboratory, Lexington, MA, USA

ABSTRACT

Avalanche Photo Diodes (APDs) have traditionally been used as detectors for wavefront sensing in curvature adaptive optics such as PUEO, the CFHT AO system. Passively quenched APDs are robust but have low QE (~40%), while actively quenched APDs can have much higher QE, but have been known to fail. Due to the cost of APDs, a CCD-based alternative appeared very attractive, especially when a large number of sub-apertures are required. The FlyEyes project was conceived to compare the performance of the backside-illuminated CCID-35 CCD detector with an array of APDs, used in an operational and well-characterized curvature wavefront AO system. Upgrades have been proposed for PUEO at various occasions and the CCID-35 was envisioned to replace an array of expensive APDs thus providing a cost-effective means of converting PUEO to a higher-order system. This paper reports on the performance of FlyEyes in PUEO.

Keywords: CCD, adaptive optics, wavefront sensing

1. INTRODUCTION

Curvature wavefront-sensing adaptive optics continues to be used and developed with excellent results at many facilities; *e.g.* MACAO, SINFONI, CRIRES at ESO, NICI at Gemini and C-188 at Subaru (Racine, 2006). A clear advantage of curvature wavefront sensing is its normalized intensity measurement scheme, which allows single pixel photon counting detectors for each subaperture and avoids the complicated optics necessary to generate and measure an image, as in a Shack-Hartman sensor. Avalanche Photo Diodes (APDs) have traditionally been used as detectors for curvature WFS, but their quantum efficiency (on the order of 40% for passively quenched APDs), their cost and failure rate (particularly for actively quenched[1] APDs), suggests that developing a CCD based detector for curvature sensing would be a useful endeavor. CFHT was eager to test such a system in anticipation that its user community should decide to upgrade its current AO system PUEO (Lai *et al.*, 2003, Lai, 2004). This led to the development of the FlyEyes detector which consists of two fiber-fed CCID-35 CCD arrays inside a dewar, and was intended for direct comparison with the APDs in PUEO as a swappable unit (Cuillandre *et al.*, 2003; Ho *et al.*, 2004, 2006). This paper describes the final system as integrated in PUEO and the results of on-sky testing.

[1] Passively quenched APDs are more robust. There have been zero failures with such devices in PUEO during 14 years of operation. However, actively quenched APDs can have a much higher QE, approaching 90%.

1.1. PUEO

The CFHT adaptive optics system, PUEO, has been in service since first light in 1996 and continues to see routine usage. A full description of PUEO and its performance can be found in Rigaut *et al.*, 1998. PUEO is based on curvature wavefront sensing with a 19-element bimorph deformable mirror (DM) and 19 passively quenched APDs. Light from the wavefront is divided into 19 sub-pupils by a lenslet array and fed via optical fibers to the APDs, which do the photon counting. FlyEyes replaces the APDs with two CCID-35 CCD detectors and an *SDSU2* controller. The optical fibers are removed from the APDs and rerouted to the CCID-35s. The CCID-35 detectors, developed at ESO and MIT/LL, were specifically tailored for use in curvature wavefront sensing (Beletic *et al.*, 2000; Dorn, 2001). A block diagram of PUEO illustrating how the CCID-35s integrate into PUEO is shown in Figure 1. A more detailed explanation of the FlyEyes concept is given in Cuillandre *et al.*, 2003 and Ho *et al.*, 2001.

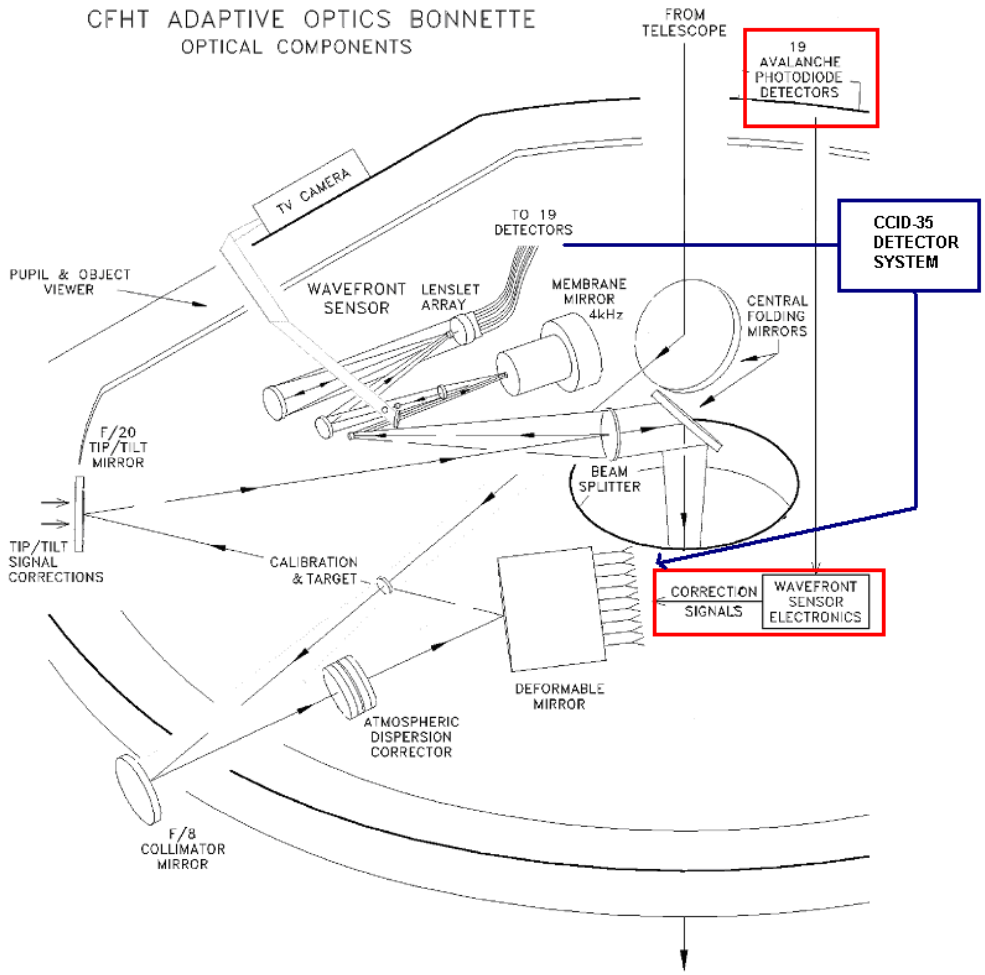

Figure 1: *The APD and CCID-35 paths are shown in this diagram of PUEO. The fibers are disconnected from the APDs and connected to the CCID-35. Instead of the digitized sum and difference counters from the analog WFS electronics, the real time computer now receives values from a dedicated interface board.*

1.2. CCID-35

The CCID-35 device was developed by the European Southern Observatory (ESO) in collaboration with the MIT-Lincoln Labs fabrication facility (Beletic *et al.*, 2000; Dorn, 2001). One of its unique design features is the "storage" areas on either side of the imaging array that are used to integrate charge from the intra-focal and extra-focal images used in curvature wavefront sensing. Having the storage areas eliminates

the need to read out the images at each half cycle of the membrane mirror intra and extra-focal modulation (4 kHz in PUEO). The images can be clocked out at the full 1 kHz sampling rate, or at a lower divisor of 2 rate (*e.g.* 500 or 250 Hz) when observing faint guide stars.

The curvature sensing area of the CCID-35 consists of 8 columns nominally[2] divided into 10 cells, with an additional 8 cell column that can be used for tip/tilt sensing (not used in CFHT PUEO), Figure 2 (top). Nominally, each cell consists of a 20 x 20 pixel imaging area (18 x 18 μm sized pixels). Each column has its own serial output register and output amplifier allowing rapid readout of the array. Figure 2 (bottom) shows a diagram of the unit cell. Note that the maximum acceptable read noise must be less than 2 electrons for the CCID-35 to provide a viable replacement for APDs. Reinhold Dorn successfully developed and tested a system at ESO with readout noise of less than 2 electrons using front illuminated versions of these devices (Dorn, 2001). The detectors are operated at –100 C. Dark current is not a concern given that exposure times are always less than 4 msec.

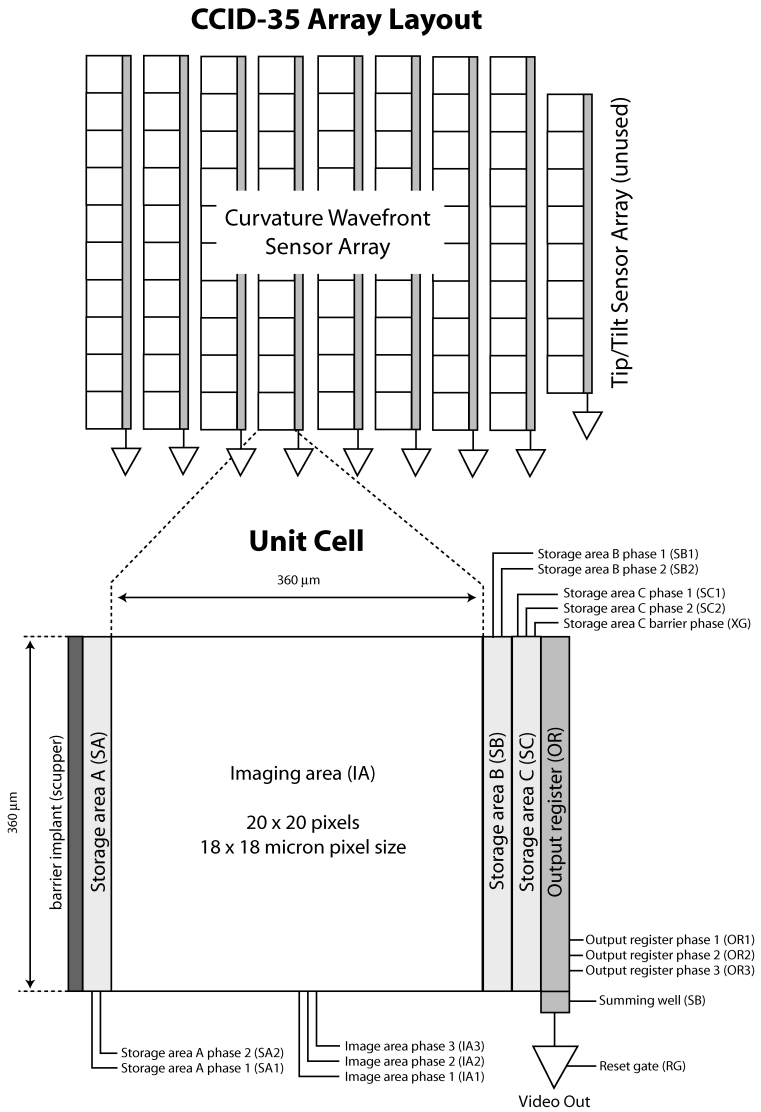

Figure 2: *Architecture of the CCID-35 wavefront sensing CCD. Top: Array layout of 10x8 cells. Bottom: unit cell.*

[2] The number of rows in each cell is arbitrary as this is defined by the vertical binning ratio. To obtain a square aspect ratio, there are 20 rows in each cell for a total of 220 rows in the CCD.

The device uses three-phase clocks for charge transfer. Storage areas SA and SB store the charge for the half-cycle intra-focal and extra-focal images. The storage area SC is used to temporarily hold the charge as one half-cycle image is clocked out through the serial output register. Charge is binned into a super-pixel at the summing well before being output at the source follower amplifier.

The need for the storage area SC may not be immediately obvious as the output register could be used to store the charge to be read out. However, since there may in general be several intra/extra-focal cycles between each sampling of the intra/extra-focal signals, the storage register SC is required to store the "A" phase signal during completion of the readout of the previous "B" signal phase located in the output serial register.

2. FlyEyes constraints and design

FlyEyes was designed with the following constraints:

- maintain the current AO control loop performance (>80 Hz loop bandwidth at 1 kHz sample rate),
- use the existing software, hardware and interfaces,
- make no modifications to the existing hardware (system must be able to be restored to its original condition) and
- provide the capability to switch between APDs and the CCID-35 so that side by side comparison testing can be done if not during the night, at least on consecutive nights.

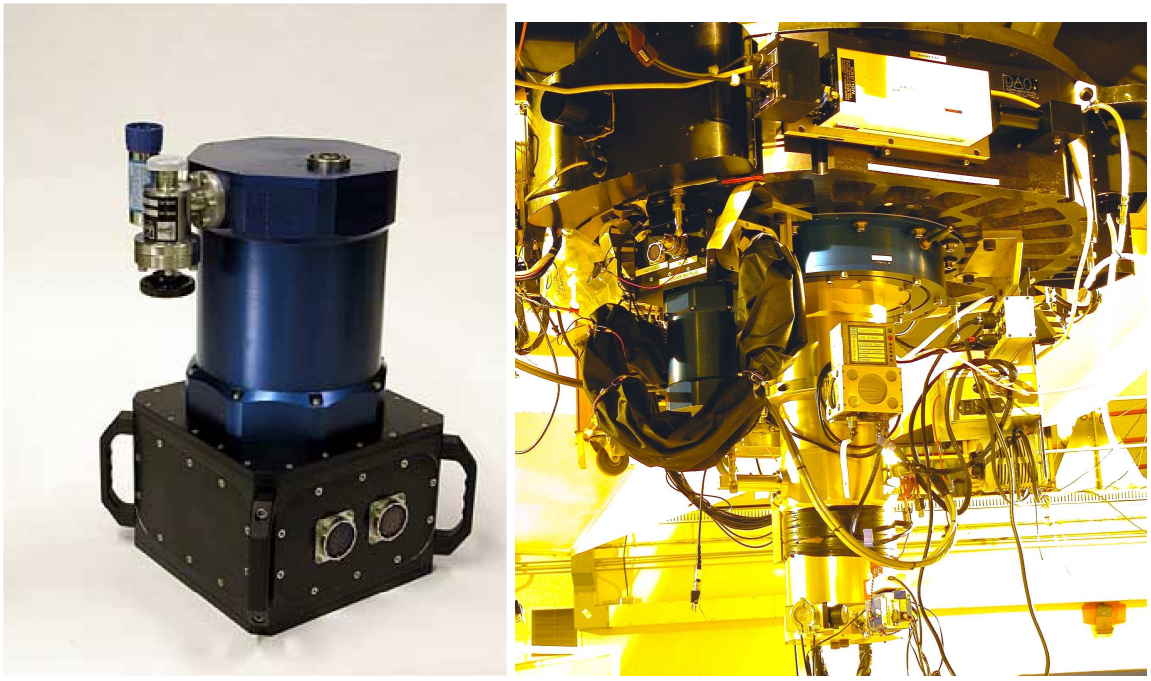

Figure 3: *Left, FlyEyes dewar. Right, mounted on PUEO (black ring-like structure at top of picture); gold dewar is the KIR scientific imaging camera.*

A picture of the system on the telescope is presented in Figure 3. Two CCID-35s are mounted in a liquid nitrogen cooled cryostat. Light from the lenslet array is brought into the cryostat via optical fibers. A *SDSU2* controller from *Astronomical Research Cameras, Inc.* provides the clocks and biases for the CCDs. Four video processor boards with dual channels handle the amplification and digitization of the 8 video channels from the CCD (Only 19 cells distributed over 4 columns are used in PUEO-FlyEyes). The *SDSU2*, which sits next to the cryostat mounted on the outside skin of the AO bonnette, transmits the readout data via fiber to the data acquisition PC in the computer room (roughly 70 meters from the telescope). A custom interface board ties in the existing interfaces to the *SDSU2* controller and data acquisition PC. This board performs address and control signal multiplexing between the digital I/O board

in the data acquisition PC and the existing wavefront sensor board (WFS). It also generates a sync signal from the 4 kHz clock which is used to synchronize timing patterns between the *SDSU2* controller and the membrane mirror.

The data acquisition PC is a dual processor, 2 GHz machine running real-time Linux. The PC processes the readout data from the *SDSU2*, which are summed and differenced and then made available to the *LaserDot* real-time computer (RTC) through the custom interface board. The *LaserDot* RTC reads and normalizes the intensities, computes the control matrix and outputs actuator drive commands to the deformable mirror.

2.1. Fiber bundle

As briefly mentioned in Section 1, the fibers are disconnected from the APDs and rerouted to the CCID-35 cryostat through a vacuum feed-through flange. Internal fibers direct the light onto the CCID-35 detector.
By far the most challenging aspect of the project was construction of the optical fiber bundle. The bundle required a minimum 19 fibers, one per each APD channel. The CCID-35 supports 80 fibers, one per each unit cell, much more than needed for PUEO. Building an 80-fiber bundle was deemed overkill so a 54-fiber bundle was settled upon. This provided a sufficient number of spares and also an opportunity to gain experience in constructing and testing a large fiber bundle, similar to the one anticipated for a PUEO upgrade. The fiber used was identical to that used to guide light to the APDs in PUEO; a 100 μm core diameter, low OH hydrogenated *CeramOptec* step-index fiber with a numerical aperture of 0.22, 120 μm cladding, 140 μm polyamide 1st coat and 250 μm epoxy 2nd coat. The second epoxy coat was removed on both ends to expose the polyamide coat, which is much smoother and more regular than the epoxy coat.
Two methods were considered in constructing the fiber bundle. Each involved precise positioning to match the center spacing of the unit cells, 360 μm x 560 μm. The first consisted of epoxying fibers to a metal ferrule with an array of 145 μm holes spaced 360 μm x 550 μm, as shown on *Figure 4*. The second utilized silicon v-grooves blocks to form a fiber stack. V-grooves in the spacers were etched to match unit cell spacing, *Figure 5*. Ultimately the silicon v-groove method was chosen simply because the v-grooves had already been fabricated and were available.

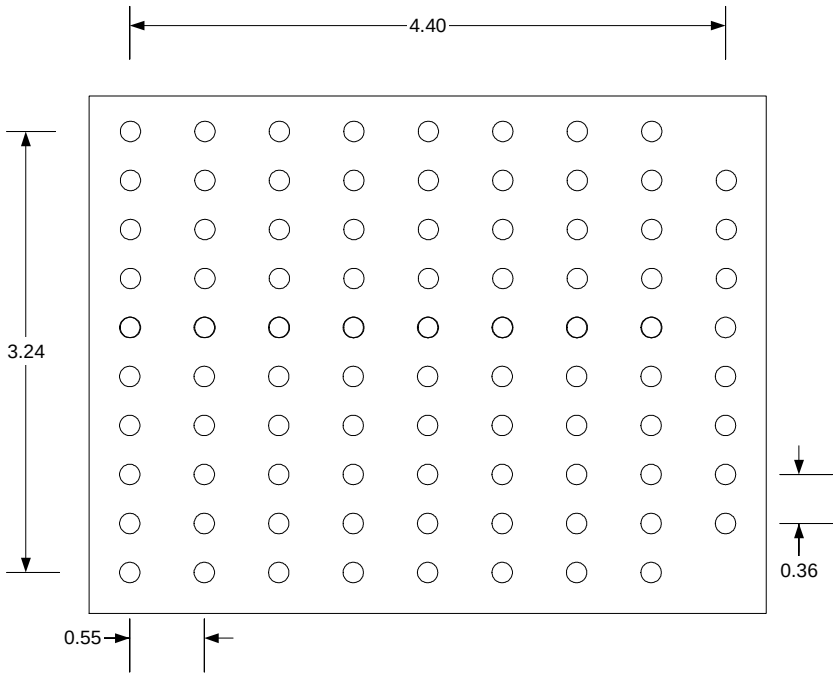

Figure 4: *Ferrule hole pattern (dimensions in mm).*

Fixtures were developed to align and hold the fibers and v-grooves in place while bonding the fibers. *Tra-bond F113* epoxy was used by virtue of its good wicking characteristics and hardness when cured to allow for optical polishing.

Alignment of the individual silicon v-groove blocks proved to be very difficult. The fiber bundle was aligned by registering the cleaved edges of the v-groove blocks. Unfortunately the cleaved edges were not identical or sufficiently consistent, which resulted in shifts in the fiber position from one row to the next. This offset can clearly be seen in the photograph of the bundle shown in *Figure 6* as well as the CCID-35 image of the light output from the individual fibers shown in *Figure 10*.

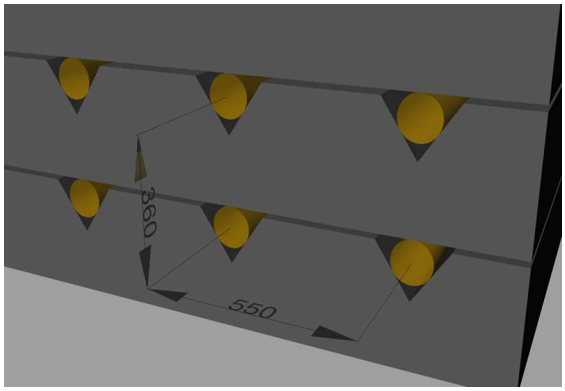

Figure 5: *Stacked silicon v-groove spacers.*

The metal ferrule approach would have provided a more precise fiber bundle and will be probably used should PUEO be upgraded. Electrical Discharge Machining (EDM) can easily produce a ferrule with an array of 145 μm conical holes at 360 μm x 550 μm spacing at relatively low cost.

The other challenge was positioning the fiber bundle above the CCID-35 surface to obtain a spot size that would fit within the unit cell while avoiding interference with the bond wires on the device. The fiber bundle had to be centered to within a few tens of microns in X, Y and θ. An adjustment mechanism designed by GL Scientific using a two pairs of wedges provided for ±600 μm to 700 μm in X and Y, and several degrees of rotation in θ. The height of the bundle above the face of the CCD (the Z direction) was fixed and set to ~200 μm in the mount. There were no provisions for adjustment on the Z axis, although shims could have been used to increase the spacing between the fiber bundle and surface of the CCID-35.

The fiber bundle was installed with the CCID-35 operating at room temperature in full frame imaging mode (*e.g. Figure 10*). Light was injected into the fibers and the CCD was read out in real-time to provide a streaming video image of the fiber spots. Since there was no way of knowing the alignment of the fiber bundle to the CCD other than through the CCD image itself, a fair amount of caution was used during initial installation. X, Y, and θ were controlled using the adjustment mechanism provided. Z was controlled using a stack of shims that were removed, one at a time, to lower the fiber bundle toward the face of the CCD in a controlled fashion.

In the end the height of the bundle above the CCD face was close to the 183 μm estimated and the spots were fairly well centered in the unit cells. During alignment the bundle was removed and installed several times with no apparent shift along any axis. The adjustment mechanism performed well and has been stable after more than 10 cooling and warming cycles. No adjustments have been made since the initial alignment.

One drawback in the design of the fiber bundle was the vacuum feed-through. By necessity, bare fibers had to be used in vacuum and jacketed fibers outside the cryostat. This made for a fiber bundle with a very heavy and fragile end. Several fibers were broken during fabrication and installation because of this. The missing spots in *Figure 10* show the location of the broken or poor transmission fibers.

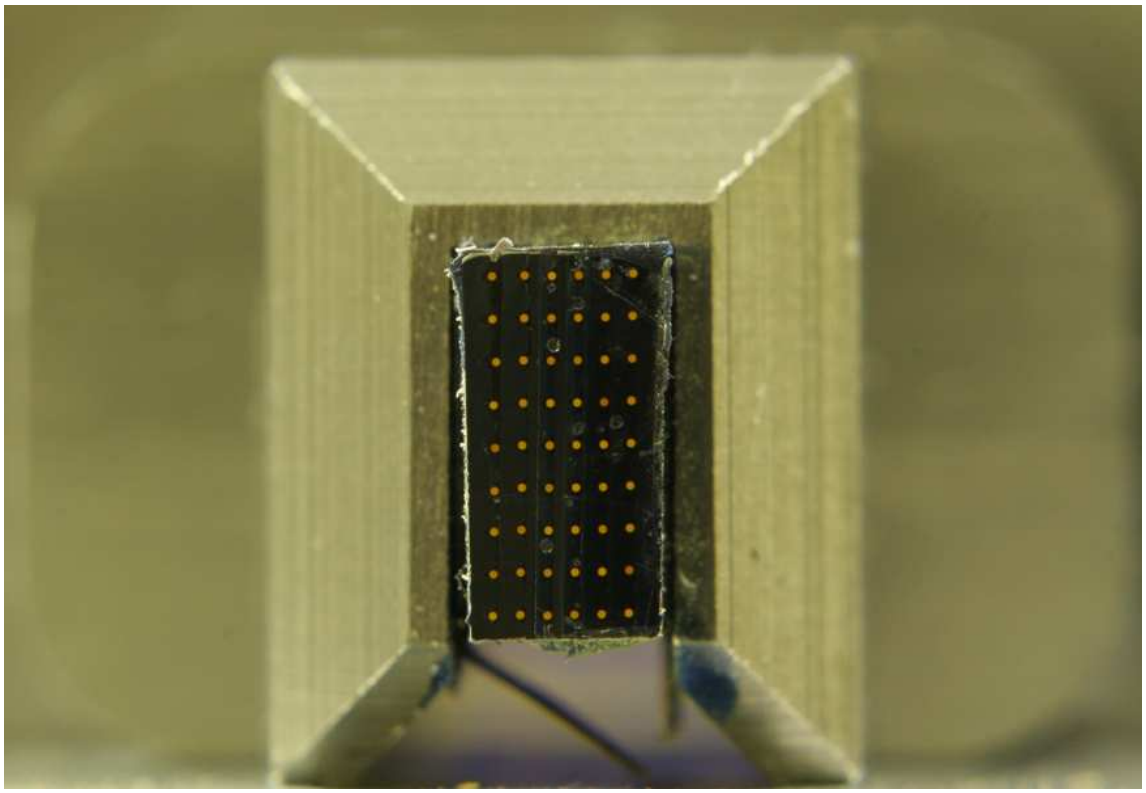

Figure 6: *End view of fibers, fiber bundle epoxied into mounting fixture.*

2.2. The interface patch board

A simple interface board was designed to receive the intra-focal and extra-focal data from the *SDSU2* controller and format it for the *LaserDot* RTC. Previously the WFS handled these tasks. The design was driven by the constraints of project, namely, that the current software and hardware interfaces had to be maintained and no modifications to the existing hardware could be made.

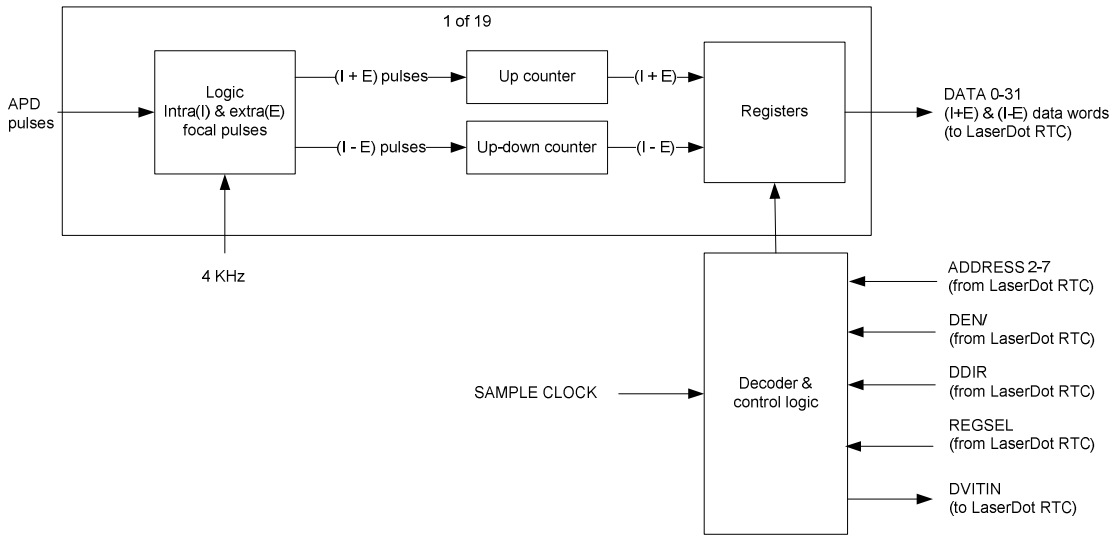

Figure 7: *WFS block diagram with APDs.*

In the original PUEO design, the intra-focal (I) and extra-focal (E) pulses from the APDs clock a multiplex of 38 (19 APDs x 2) 16- bit up-down counters. Discrete logic would combine the I and E pulses into the

sum (I + E), and difference (I - E), signals. The "sum" and "difference" signals would each clock an individual counter. The output of the counters would be latched and stored in registers on every sampling period (*e.g.* at 1 kHz). The *LaserDot* RTC addresses and reads the sums and differences for each APD in nineteen 32-bit reads and uses these to compute the drive signal to the deformable mirror.

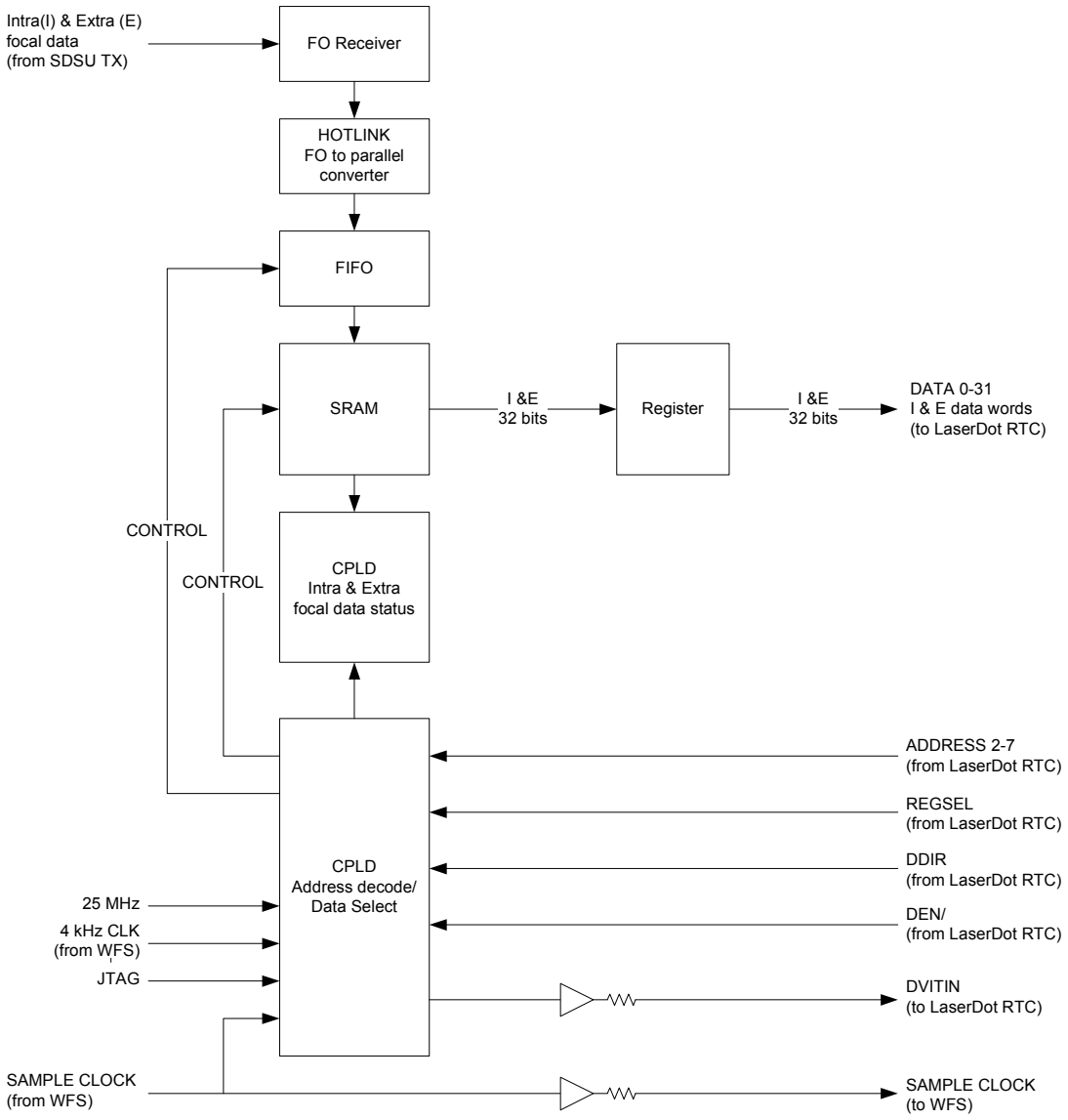

Figure 8: *Interface board block diagram.*

In the new interface board, I and E data from the *SDSU2* controller is transmitted down a single fiber and is converted into 2 parallel words using a *HOTlink* receiver/converter pair. The data words are written into a FIFO and then stored in a 32K x 8 SRAM. I and E data from 64 of 80 unit cells of the CCID35 are read regardless of whether they are illuminated with light from the fibers or not, in order to maintain consistent timing between the sampling of different cells. During the commissioning, all the operational fiber and unit cell pairs were examined by viewing the spot image and the best 19 were selected. An address decoder implemented with a complex programmable logic device (CPLD) maps the locations of the best 19 fiber spots to the original *LaserDot* addresses. By necessity the interface board uses the same input and output signals and definitions as the WFS. A pair can easily be changed if needed, for instance if its fiber got broken, by simply remapping the *LaserDot* RTC addresses to the addresses corresponding to the new pair. This is done through a JTAG port and CPLD programming software. Unlike in the original WFS, the I and

E sums and differences are not available, only the raw data. The *LaserDot* RTC addresses and reads the I and E data and computes the sums and differences in the real-time code.

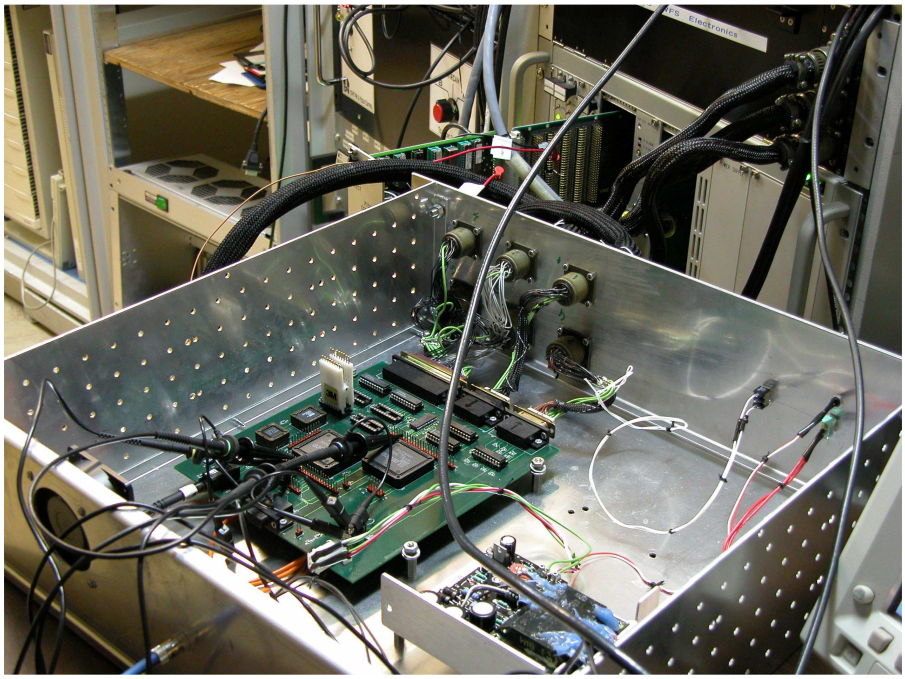

Figure 9: *The interface board plugged in the LaserDot RTC.*

If PUEO were to be upgraded with FlyEyes, all the electronics and RTC would be redesigned. The present hardware is obsolete and non-scalable. The scheme used on the interface board would not be considered since it was designed simply to interface with the present hardware. The hardware required would conceivably be much simpler than what was necessary to integrate FlyEyes with PUEO.

3. CCID-35 Characterization and Clocking

An image of the fibers on the CCD is shown in *Figure 10*. Several fibers are broken and a few CCD cells are unusable due to defect structures. For PUEO, only 19 channels are needed so this does not present a problem. The fibers selected for the signals were from the fibers in the 3 cell rows nearest the output amplifiers to minimize the time required to shift out the pixels.

In CFHT's PUEO instrument, the membrane mirror cycles between the intra-focal (I) and extra-focal (E) images at 4 kHz, however the readout of the photon counts associated with each phase is performed at 1 kHz in its highest bandwidth operation mode. When the avalanche photodiodes (APDs) are used for sensing, the system alternates 4 times per 1 kHz cycle between incrementing the I or E counters. If the sensing frequency is reduced by n octaves, then the system must alternate $4x2^n$ times between feeding the I or E counters before these are read out. The CCID-35 is clocked in such a way as to emulate this behaviour. The readout of the CCID-35 is performed as quickly as possible, within the limits necessary for maintaining low readout noise, in order to minimize the phase-lag between the readout of the intra-focal and extra-focal signals.

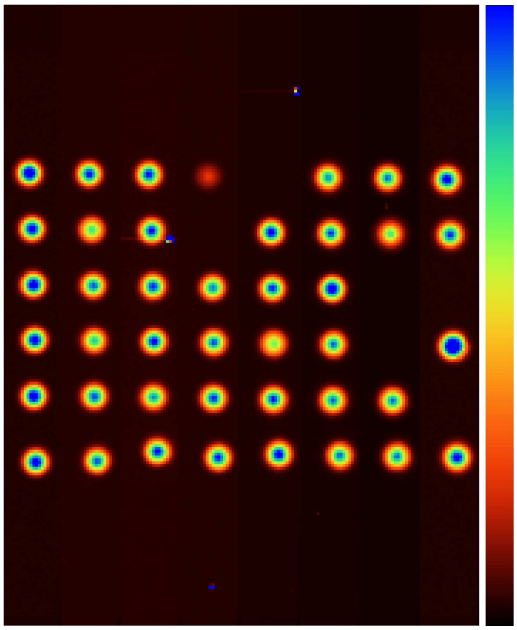

Figure 10: *Afocal image of the fiber output on the CCID-35. Note that the image includes 20 pixels of over-scan on the top edge (normally used for noise analysis). The readout direction is towards the bottom (in accordance with the architecture schematic above).*

A high-level flow-chart of the CCID-35 clocking scheme for FlyEyes is shown in *Table 1*. The *SDSU2* controller used to control the CCID-35 contains four, 2-channel video sampling cards and a dual fiber-transmitter version of the timing/interface board. Only 8 out of the 10 available cells on the device are read out. Note that the pseudo-code in Table-1 is written from the point of view of commands sent in parallel to both video boards, so that the total number of cell samples is actually twice what is shown, *i.e.* 128. The second fiber on the timing board is used to transmit pixel data to the AOB RTC through the FlyEyes interface board (Section 2.2). On the beginning of each sample period, ten 16-bit words containing 0xFFFF are sent over the pixel-data fiber as a synchronization signal detected by the FlyEyes interface board.

At 1 kHz sampling there is about 90° of phase lag between the transmission of the intra-focal and extra-focal signals. For lower sampling rates, steps 5 through 8 are repeated as necessary to obtain the desired sampling period. For example, to obtain a 500 Hz sampling rate one would perform steps 5 and 6 six times.

The unbinned readout noise for this device was previously reported by Ho *et al.*, 2006. Further tests using an alternate measurement method confirmed these results, however it was found that the noise was significantly higher when binning the pixels 20 x 20 in AO mode compared to the unbinned, imaging mode. It was found that the noise could be significantly reduced (from ~3, down to ~2 electrons RMS) by limiting the swing of the parallel and serial clocks. The optimal voltage swing was 7 V for the parallel clocks (originally this had been set to 10 V) and 6 V for the serial clocks (originally this was 7 V). The most likely explanation for the excess noise at the higher clock swings is spurious charge generation through impact ionization. Although the probability of generating charge in this manner is usually negligibly small at such small voltage swings, the large number of shifts (and fast clock edges) used when operating the device in AO mode (over 80 when sampling at 1 kHz) could lead to a significant effect. A noise transfer curve for one channel of the CCD operated in AO mode is shown in *Figure 11*. The readout noise obtained ranged from 1.9 to 2.7 e^- RMS, with an average noise of 2.3 e^- RMS.

1 kHz	4 kHz	Actions (in order)	1 kHz	4 kHz	Actions (in order)
1		Send out synchronization word (0xFFFF x 2) *Shift SB to OR* Skip lead-in pixels Clock and sample but don't send 1 x 8 cells Clock, sample and send 3 x 8 cells Wait for 1 kHz signal to rise	5		*Shift IA to SB* Sample but don't send 4 x 8 cells Wait for 4 kHz signal to go high
2		Introduce delay to symmetrize A and B phase timings *Shift SA to SB* Clock, sample and send 4 x 8 cells Send last cell in ADC pipeline *Shift SB to OR* Skip lead-in pixels Wait for 4 kHz signal to go low	6		Introduce delay to symmetrize A and B phase timings *Shift IA to SA* Sample but don't send 4 x 8 cells Wait for 4 kHz signal to go low
3		*Shift IA to SB* Clock and sample but don't send 1 x 8 cells Clock, sample and send 3 x 8 cells Wait for 4 kHz signal to go high	7		*Shift IA to SB* Sample but don't send 4 x 8 cells Wait for 4 kHz signal to go high
4		Introduce delay to symmetrize A and B phase timings *Shift IA to SA* Clock, sample and send 4 x 8 cells Send last cell in ADC pipeline Wait for 4 kHz signal to go low	8		Introduce delay to symmetrize A and B phase timings *Shift IA to SA* Sample but don't send 4 x 8 cells Wait for 4 kHz signal to go low

Low clock signal
High clock signal

Table 1*: The PUEO-FlyEyes clocking sequence for one cycle of the 1 kHz clock (the highest correction bandwidth case). Time follows the numbering of the 4 kHz clock phases from 1 to 8. A "cell" refers to a binned super-pixel of size 20 x 20.*

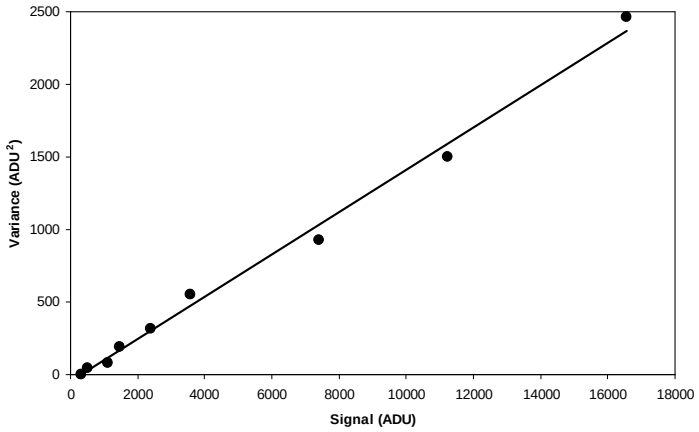

Figure 11*: Noise transfer curve for one channel of the CCID-35 operated in AO mode with 1 kHz sampling.*

4. Performance results

Although early simulations (Craven-Bartle *et al.*, 2000) show that the performance of FlyEyes should be equivalent to that of the APDs, the read-noise of a CCD introduces subtle changes in the operation of a curvature wavefront sensor.

4.1. Read noise

In photon counting detectors, the noise is integrated in the servo-loop and low frequencies are more strongly attenuated due to their improved SNR. Thus with APDs, the noise (*i.e.* the variance of the wavefront sensor signal) goes as N^{-1} with N the number of photons detected in a time interval. In a CCD on the other hand, read noise is added in every frame so the noise goes as N^{-2}, where the N photons have now been detected over many reads (in other words, the read noise accumulates in the loop). This is shown in *Figure 12*, which uses the formula for Shack-Hartmann wavefront sensors for the CCID-35, but still maintains the correct noise behavior.

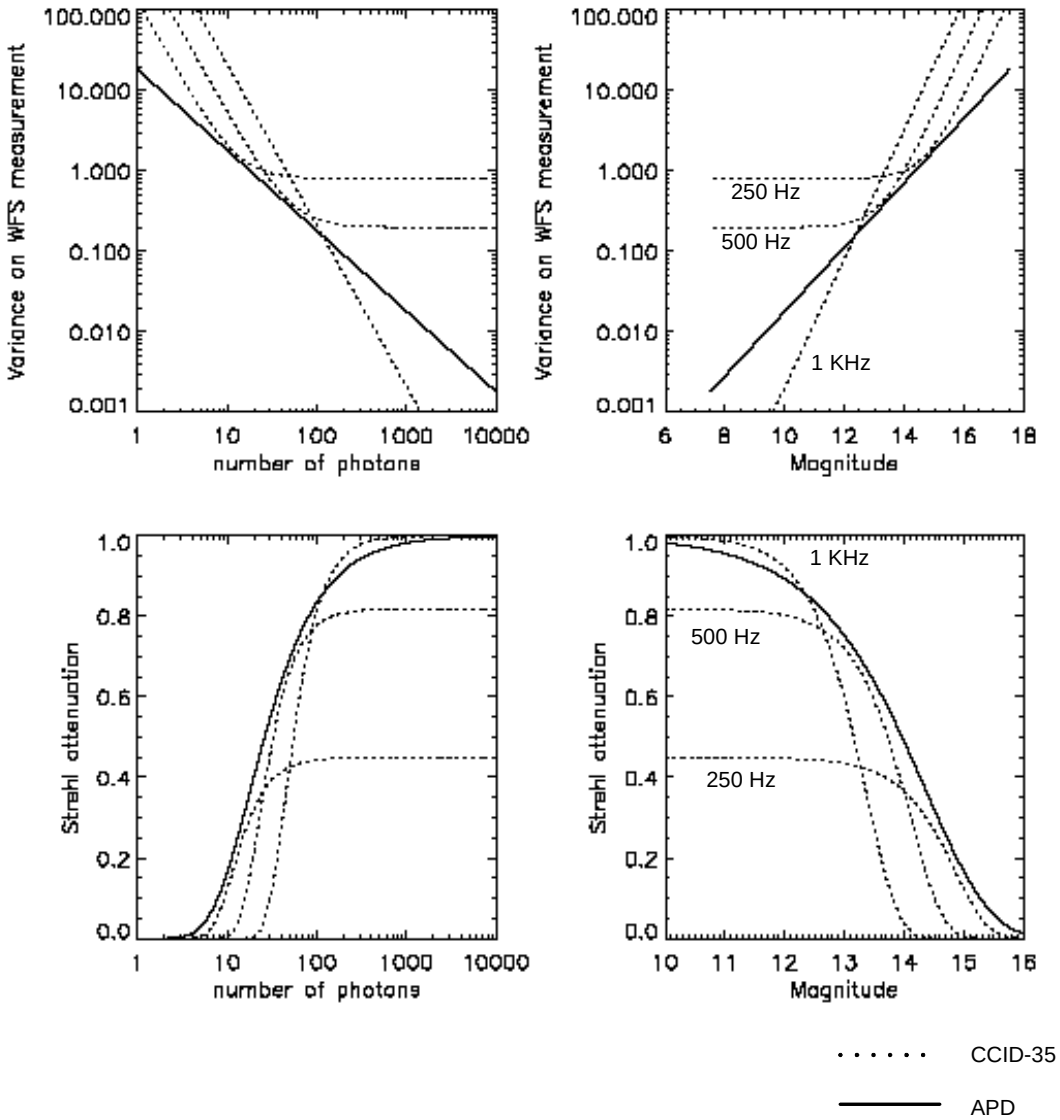

Figure 12: *Variance on WFS measurements (top) and equivalent Strehl attenuation (bottom) for incident number of photons (left) and equivalent Guide Star magnitude (right) for APDs (full line) and CCID-35 (dotted line).*

The following equation can be used to calculate the WFS measurement variance for the APDs where the photon noise dominates.

$$\sigma_{WFS}^{\ 2} = \frac{7.2}{N_{photon} * QE_{APD}} \qquad (\text{rad}^2)$$

where N_{photon} is the number of photons, and QE_{APD} is the APD quantum efficiency, 0.4 in this case. For the CCID-35, the WFS measurement variance is given by:

$$\sigma_{WFS}{}^2 = \frac{\frac{\pi^4}{3} * (\sigma_{read} * n_{pixels})^2}{(N_{photon} * QE_{CCD})^2} + \sigma_{bandwidth}{}^2 \quad (\text{rad}^2)$$

where the read noise per pixel σ_{read} is 1.8 e-, read over n_{pixels} (we assume 4), where N_{photon} is the number of photons, and QE_{CCD} is the CCID-35 quantum efficiency, assumed to be 0.9. The last term, $\sigma_{bandwidth}{}^2$ is the phase lag error. This term is required because although increasing the integration time on the WFS improves the SNR in terms of detected photons, it does so at the expense of the temporal error, determined by the Greenwood frequency and the loop correction frequency. In the example shown in Figure 12, the CCID-35 is operated at 1 kHz with no phase lag error, at 500 Hz (double the number of photons per exposure) but with a 0.2 rad^2 phase lag error and at 250 Hz with a 0.8 rad^2 phase lag error. This illustrates that on the bright end, a high sampling frequency is desirable to match the APD performance, despite the gain in QE, while at the faint end, the APD performance level can be emulated by lowering the sampling frequency. These simulations imply that by carefully adjusting the wavefront sensor frequency, the performance of PUEO should remain unaffected when using the CCID-35.

4.2. Low flux levels

Another difference introduced by the finite read noise of the CCD appears at very low flux levels. The wavefront sensor estimates the local wavefront curvature by estimating the contrast between the intra/extra-focal images:

$$C = \frac{I_{\text{int}ra} - I_{extra}}{I_{\text{int}ra} + I_{extra}} \propto \nabla^2 \varphi$$

In the absence of read noise, the denominator can only be zero when the numerator is also zero, and so if no photons are detected during an integration cycle, we set C to zero. But in the presence of read noise, the denominator can be null or negative once the bias level has been subtracted out (it turns out to be less of a problem if it is negative rather than null). Various schemes were simulated to try to reduce the instability and improve poor performance at low flux. These included: clipping the denominator to positive values only, using a running average on the denominator and adding a bias to the detected intensities. Results of Monte Carlo simulations using the IDL code `simul.pro` developed by François Rigaut (private communication) are presented in *Figure 13*.

It is apparent that a running average in the denominator only marginally improves the performance, if at all. Adding a bias seems to have a more important effect: the bias subtracts out in the numerator, but adds a constant term in the denominator, effectively lowering the loop (or integrator) gain. As all the simulations were run with a constant loop gain of 0.6, adding a bias to the detector signal improves the results of the simulations at low photon flux. However, PUEO uses a modal control that self-optimizes in closed loop and applies the gain that reduces the residual phase variance. Therefore when this method was tried on the sky, it was not found to improve performance.

Sky testing revealed that the detailed modeling presented above, which should have predicted the optimal wavefront sensing frequency as a function of the guide star brightness, did not take into account the varying sky conditions. Even accounting for r_0 fluctuations did not allow us to definitively and repeatedly demonstrate an improvement of performance on faint sources at lower sampling frequencies. This may have been due to a rapidly varying τ_0. Anecdotally, during a short period PUEO with FlyEyes was delivering 25% Strehl ratio in K band guiding on a magnitude 15.8 star (see *e.g. Figure 15*.)

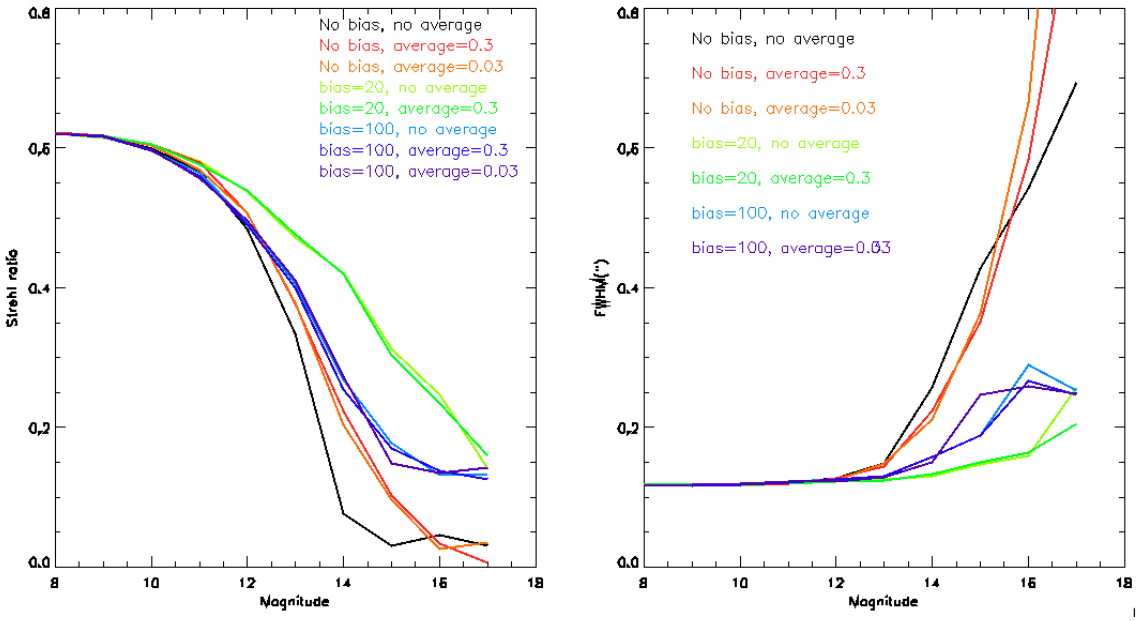

Figure 13: *Simulated Strehl and FWHM as a function of guide star magnitude, with bias or running average in denominator to prevent loop instabilities. A bias of 20 seems to provide the most improvement in this case.*

4.3. Bright star performance

FlyEyes was tested on AOB on the nights of April 24th-26th 2007, February 25th-27th 2008 and a comparison run with the APDs took place on December 17th-18th 2007. The comparison tests indicate that the bright star performance is unaffected, as shown in *Figure 14*.

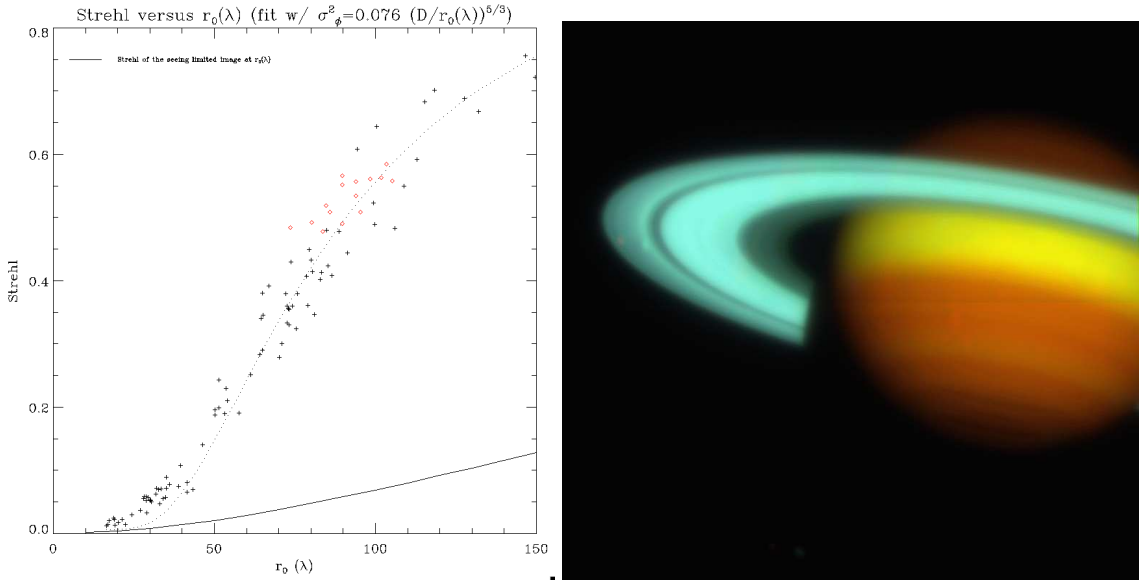

Figure 14: *Bright guide star performance, showing the delivered Strehl ratio as a function of $r_0(\lambda)$; original 1996 integration data, black crosses, April 2007 data, red diamonds. Right: Saturn, observed on April 27th 2007 at UT 9:00; Wavefront sensing with FlyEyes was performed on Dione, which was magnitude 10.2 at the time.*

The plot on the left shows the delivered Strehl ratio as a function of the r_0 at the wavelength of observation. The black crosses show the original 1996 integration data, which consisted of more than 300 observations

of stars at all wavelengths in varying conditions (Rigaut *et al.*, 1998). The red diamonds show the dynamic Strehl ratio measured on images obtained with KIR (the science camera) in April 2007 as a function of the r_0 estimated from the wavefront sensor data and they lie right at the expected value. Also shown is a picture of Saturn obtained on April 27th at 9:00UTC while guiding on Dione, which was magnitude 10.2 at the time. Images were obtained in J, H and K bands and were stacked to produce the image in *Figure 14*. We experimented with the various schemes described in section 4.2 but found that the loop remained most stable with no modifications (*i.e.* no bias nor running average).

4.4. Faint star performance

The comparison with APDs turned out to be more difficult than anticipated due to varying seeing (and τ_0) conditions. Nonetheless, by recording and correcting for the r_0 estimated by the wavefront sensor data, we were able to confirm that the performance was not noticeably degraded by using FlyEyes instead of the APDs.

The modal control of PUEO works by estimating the input phase power spectrum from the measured residual power spectrum of the WFS measurement and using a model of its well-known and characterized transfer function[3]. Once the input spectrum is estimated, the loop gain which minimizes the integral of the product of this spectrum multiplied by the associated error transfer function is applied to the loop and the whole process is repeated; the loop gain thus self-optimizes in closed loop. This process depends on the transfer function used, and in PUEO, the temporal characteristics of the integrator and the photon noise make this a straightforward process. We were unable to implement a full modal control for FlyEyes as it would have required modeling (or measuring) the transfer functions and the read noise for the different sampling frequencies and loop gains with little certainty in their accuracy. Instead, we ran our tests with either the modal control enabled (assuming the simplest loop integrator, but neglecting read noise, thus probably not optimized) or with zonal control enabled, setting the gain manually. This made the testing cumbersome, but a sufficient number of data points were collected to see trends emerging, as shown in *Figure 15*.

The left column shows the number of detected photons translated into magnitudes as a function of the quoted guide star magnitude. Some spread can thus be expected due to varying spectral type and photometric conditions. The zero point of 18.5 is the same for FlyEyes as it is for the APDs (Rigaut *et al.*, 1998). The black symbols are for 1 kHz data, red for 500 Hz and pink for 250 Hz. Note the read noise seems to appear at magnitude 15.4 at 1 kHz.

The middle column shows the raw Strehl ratio, as measured on the KIR detector as a function of the guide star magnitude. The spread is understandable as there is no accounting for either the actual detected number of photons or the r_0 at the time of the observations. The top panel shows modal control and the bottom panel shows zonal control; in both cases the black diamonds represent the 1 kHz sampling frequency, the green crosses 500 Hz, and the yellow ones 250 Hz. The spread is such that it is hard to infer any quantitative assessment of the performance, although qualitatively, it appears that lowering the sampling frequency improves the performance above magnitude 11.

The right column shows the final result, after having accounted for the static Strehl ratio, the number of detected photons and the r_0 at the time of the observations. The small black diamonds are the dynamic (*i.e.* corrected only for static aberrations) Strehl at 1 Khz, leaving the spread unchanged, but renormalized. The red crosses show the same data corrected for r_0, and can thus be interpreted as Strehl attenuation. The green crosses show the Strehl attenuation at 500 Hz and the yellow ones at 250 Hz; one will note that the spread of the data has been reduced. A best-fit model to the data is shown by the blue curves (the dashed curves show by how much the 1 kHz curve would be displaced if halving the sampling frequency simply doubled the number of photons, assuming a negligible phase lag error). There is a fair agreement especially for the 250 Hz data at the faint end. Also note that on bright (magnitude 12) stars, the zonal control performs much more poorly at 500 and 250 Hz than at 1 kHz, as was expected (*e.g. Figure 12*). However, in modal

[3] By definition, the measured residual spectrum is the input spectrum attenuated – multiplied by – the error transfer function

control at high flux, the read noise is small compared to the photon and lag noise, so the loop gain optimizing algorithm seems to be doing the right thing, improving the performance by increasing the loop gain so as to compensate the lower loop frequency. Nevertheless, the spread in the data, probably due to varying temporal conditions of the atmosphere, prevented us from finding a clean cross-over of performance for various sampling frequencies as was expected from the model (*Figure 12*), nor was sufficient precision obtained to compare FlyEyes to the performance of the APDs. Quantitatively, we can point out that we expect a Strehl attenuation of 50% due to the guide star brightness at around magnitude 15.

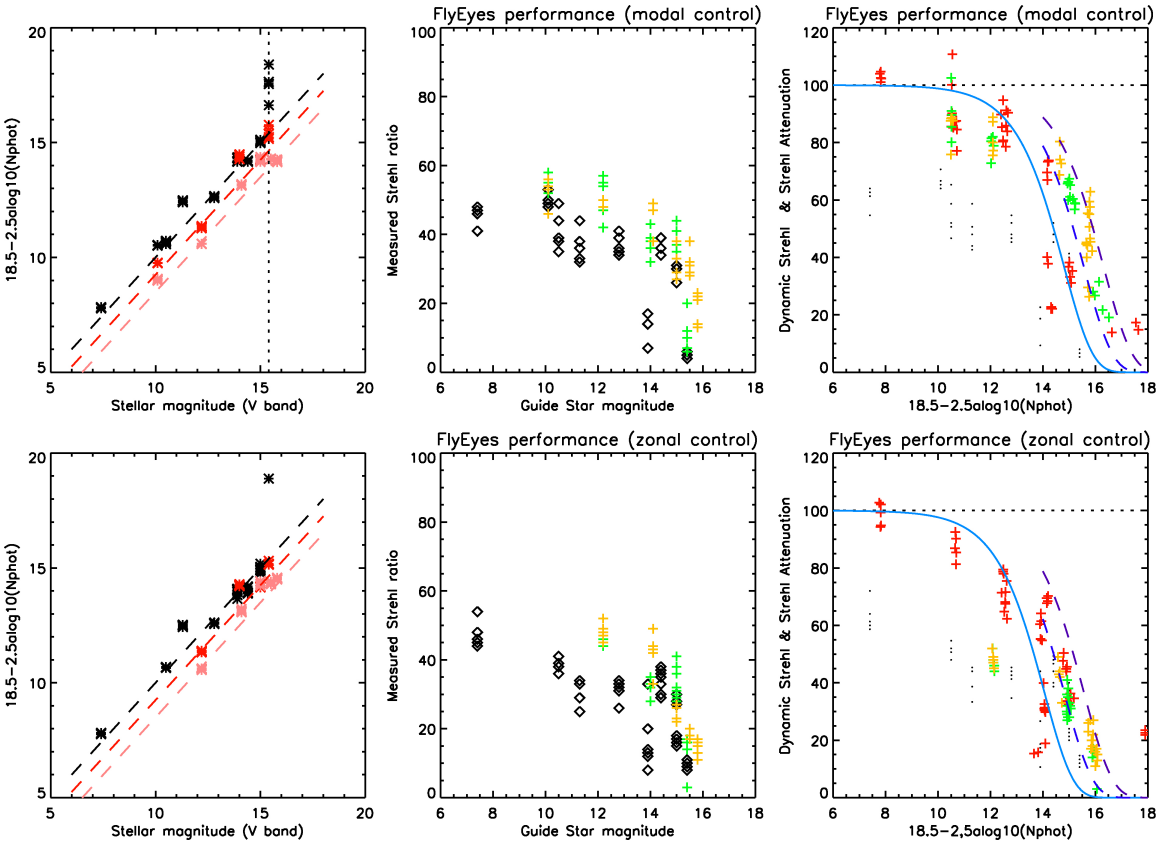

Figure 15: *FlyEyes performance as a function of guide star magnitude. Left: photometry. Center, recorded Strehl. Right: Strehl attenuation, corrected for r_0. Top row is with PUEO modal control, while the lower row is for zonal control at various gains.*

Although this characterization is enough to confirm that a detector such as the CCID-35 can be used for curvature wavefront sensing in an astronomical setting without any loss of performance with respect to APDs, from an operational standpoint it does not allow us to determine and automate the sampling frequency and loop gain for optimal performance. Since the demand on PUEO has decreased, there is no strong motivation to replace the APDs with FlyEyes, although an upgrade of PUEO is now easily within reach, should the astronomical community demand it.

5. Conclusions

We have described the FlyEyes experiment, which used a CCID-35 CCD detector as an alternate detector to PUEO's APDs. The CCID-35 has better quantum efficiency than the passively quenched APDs used in PUEO, but introduces a 2 electron read noise penalty. FlyEyes was successfully integrated and tested with PUEO using a fiber bundle to divert the light from the APDs to a CCID-35 detector. An interface board was implemented to send the WFS measurements to the Real Time Computer. On-sky operation was achieved on bright stars ($V < 10$). On fainter stars ($10 < V < 16$), different schemes were attempted to reduce the effects of the read noise, but none showed definitive improvements under our test conditions.

FlyEyes performed at least as well as the APDs, although varying atmospheric conditions prevented us from obtaining repeatable performance as a function of guide star magnitude. Anecdotally, FlyEyes provided 25% Strehl ratio on a 15.8 magnitude star; a Strehl attenuation of 50% can be expected when the guide star is magnitude 15. It would be desirable from an operational standpoint to determine the optimal sampling frequency as a function of guide star magnitude. Our dataset was not accurate enough to determine the cross-over sampling frequency for optimal performance. The demand for PUEO is steady but low, so there is no strong incentive to use FlyEyes as a replacement for the APDs as this would require further integration and characterization effort. However, should the CFHT user community decide that an upgrade of PUEO is necessary, the perfect detector is ready and waiting…

6. References

Beletic, J.W., Dorn, R.J., Craven-Bartle, T., Burke, B., (2000), "*A new CCD designed for curvature wavefront sensing*", Optical Detectors for Astronomy II: State-of-the-Art at the Turn of the Millenium. 4th ESO CCD Workshop.

Craven-Bartle, T.V., Dorn, R.J., Beletic, J.W., (2000), "*Computer simulation comparison of CCDs and APDs for curvature wavefront sensing*", Proc. SPIE, **4007**, 444.

Cuillandre, J.-C., Beletic, J.W., Dorn R.J., Luppino, G.A., Isani, S., Gorceix, N., Lai, O., Craven-Bartle, T.V., Burke, B.E., Ménard, F., (2003), "*FlyEyes: a dual CCD detector system for CFHT PUEO NUI's wavefront sensor*", Proc SPIE **4839**, 272.

Dorn, Reinhold J., (2001), "*A CCD based curvature wavefront sensor for adaptive optics in astronomy*", Ph.D. dissertation, Ruperto-Carola University of Heidelberg, Germany.

Ho, K., Cuillandre, J.-C., Puget, P., Salmon, D., Lai, O., Beletic, J.W., Luppino, G., Dorn, R., J.; Burke, B., (2004), "*Update report on FlyEyes: a dual CCD detector system upgrade for PUEO*", Proc SPIE **5499**, 395.

Ho, K. J., Cuillandre, J.C., Lin, C.J., Benedict, T., Lai, O., Ward, J., Salmon, D., Luppino, G., Beletic, J., Dorn, R., Puget, P., Burke, B., Wang, S.Y., (2006), "*FlyEyes: Integrating CCID-35 into PUEO AO system at CFHT*", Proc. SPIE, **6276**, 62761G.

Lai, O. , Ménard, F., Cuillandre, J.-C., (2003), "*PUEO NUI: feasible and fast upgrade of the CFHT Adaptive Optics system for high dynamic range imaging*", Proc SPIE **4839**, 659.

Lai, O. (2004), "*Sawn song for an Owl: the scientific cases for Pueo Nui eProceedings*". eProceedings CD Rom of Grenoble Workshop. Editor: O Lai.

Racine, R., (2006), "*The Strehl Efficiency of Adaptive Optics Systems*", *Publ. Astron. Soc. Pacific,* **118**, 1066.

Rigaut, F.J., Salmon, D.S., Arsenault R.A., Thomas, J., Lai, O., Rouan D., Véran J.-P., Gigan, P., Crampton, D., Fletcher, J.M., Stilburn, J., Boyer, C. and Jagourel, P., (1998), "*Performance of the Canada-France-Hawaii Telescope Adaptive Optics Bonnette*", *Publ. Astron. Soc. Pacific*, **110**, 152.